Proceedings of the ASME 2023 42nd International Conference on Ocean, Offshore and Arctic Engineering
OMAE2023
June 11-16, 2023, Melbourne, Australia

OMAE2023-104877

RETRIEVAL OF OCEAN WAVE SPECTRA FROM X-BAND MARINE RADAR IMAGES USING INVERSION SCHEMES BASED ON AUTO-SPECTRAL ANALYSIS

Gowtham Radhakrishnan
Department of Marine Technology,
SFI MOVE, NTNU,
Trondheim, Norway

Bernt J. Leira
Department of Marine Technology,
SFI MOVE, NTNU,
Trondheim, Norway

Zhen Gao
Department of Marine Technology,
SFI MOVE, NTNU,
Trondheim, Norway
NAOCE, SJTU,
Shanghai, China

Svein Sævik
Department of Marine Technology,
SFI MOVE, NTNU,
Trondheim, Norway

Konstantinos Christakos
Department of Marine Technology,
SFI MOVE, NTNU,
Trondheim, Norway
MET, Bergen, Norway

ABSTRACT

Estimation of ocean wave conditions is extremely crucial for the planning and execution of demanding marine operations. Further, the Response Based Decision-Making requires accurate wave inputs to derive the responses using a numerical model. The X-band marine radars, installed on top of the vessels, are cost-effective means to assess the incoming wave field. Dedicated full-scale measurements were conducted using the research vessel Gunnerus in the Breisundet field, located on the west coast of Norway. After interaction with the ocean waves, the electromagnetic waves from the radar are backscattered based on the Bragg scattering mechanism. The radar digitizes the backscattered signal in the form of intensity images. 3-Dimensional (3-D) Fast Fourier Transform (FFT) was adopted to convert the temporal sequence of backscattered images to the wavenumber-frequency representations. The current velocity components estimated using the least-squares approach showed better agreement with the buoy-based current measurements. Then the wave-related components were extracted based on the linear wave dispersion relationship. Subsequently, the spectra were corrected for the shadowing effect using modulation transfer functions. Finally, the radar-based wave measurements were scaled using the nearby wave buoy records. The estimation of wave spectra improved considerably after the application of the Modulation Transfer Function (MTF). The spectra at the mid-range gave the best results when studying the effects due to range dependency. The spectra processed from radar images were validated using wave buoy measurements.

Keywords: X-band marine radars, wave buoy, 3-D FFT, wave spectrum, MTF

NOMENCLATURE

HF	High-Frequency
R/V	Research Vessel
RBDM	Response-Based Decision Making
FFT	Fast Fourier Transform
IFFT	Inverse Fast Fourier Transform
MTF	Modulation Transfer function
SAR	Synthetic Aperture Radar

1. INTRODUCTION

For proper planning and safe execution of a marine operation, it is deemed crucial to consider the prevalent wave conditions at the operational site for decision-making. Traditionally, the forecasted wave statistical parameters from weather models have been utilized for operational decisions. Arriving at critical decisions in real-time requires precise

knowledge about the incoming wave field and critical events, which in turn requires wave-field measurement techniques in real-time. The information on both phase-resolved wave elevations and directional spectra prevalent at the operational site is crucial for predicting the vessel responses within the framework of Response-Based Decision Making (RBDM) methodology.

Several on-field measurement techniques, like deploying in-situ sensors, coastal HF-frequency radars, marine radars, and satellite- and air-borne-based ocean-mapping techniques are already in practice for measuring the wave climate. The in-situ sensors include pressure sensors, wave buoys, etc., deployed directly in the ocean space to measure waves [1]. The Synthetic Aperture Radar (SAR) images from the SAR mission can also be processed to obtain the wave elevation and directional spectra [2]. However, such instruments do not offer information about waves at all temporal and spatial scales across the globe. Especially, in-situ sensors such as wave buoys are limited to measuring the wave field at a specific point in space which limits the applicability of the data, e.g., investigation of spatial wave coherence and homogeneity needs several wave buoys which is expensive [3]. Alternatively, X-band radars installed on marine vessels offer a convenient means to measure the incoming wave field at a spatial resolution of 3-5 km and at a high temporal resolution. Since they are installed on the vessel/platform itself, realistic wave conditions could be obtained at the operation site itself. Its working principle is based on Bragg's resonance phenomenon. The electromagnetic waves from the radar are scattered by the sea surface when their order of wavelength is similar to that of the ocean waves. The radar captures waves of the order of ≥ 3 cm. The radar digitizes the backscattered signal through intensity images, from which different wave-related information can be determined. This study utilizes the backscattered intensity images collected from the full-scale trials to retrieve the wave spectra based on the inversion procedures in Borge et al. [4].

The processed wave data from the X-and marine radars will be tested for real-time applications in response-based decision support systems onboard a vessel. The decision support application includes 1) the directional wave spectra estimated at the site and the simultaneously recorded vessel motion measurements could be utilized to tune the computational model of the vessel, such that the simulated responses match the measured responses precisely, 2) the tuned model can then be used to forecast vessel responses 2-3 minutes ahead by considering the spatio-temporal evolution of the phase-resolved wave elevation estimated from the radar images.

The organization of the paper is as follows. The details on the full-scale measurements are given in Sec. 2, followed by the detailed theoretical explanation of the conversion procedures to estimate the wave frequency spectra from radar images. The estimated spectra are compared with the buoy-based spectra and the results are discussed in Sec. 3. The conclusions and future work are provided in Sec. 4.

2. MATERIALS AND METHODS

2.1 Full-Scale measurements

Full-scale wave and vessel motion measurements were conducted in the Breisundet, an exposed strait to energetic offshore waves, located on the west coast of Norway. An X-band wave radar provided by Miros was installed on the NTNU Research Vessel (R/V) Gunnerus. The measurement campaign was part of the SFI-MOVE (Marine Operations in Virtual Environments). The sole aim of the campaign is to measure the incoming wave conditions and ship motions simultaneously in order to develop Onboard decision support systems based on Response-Based Decision-Making (RBDM). The full-scale tests were conducted close to Buoy D at Breisundet. This location was selected as both wind waves and swell were present and choppy seas were observed. The swell was arriving from the open ocean and the winds blowing from Sulafjorden generated the wind sea. The buoy is a *heave-roll-pitch* (SEAWATCH WaveScan) buoy located approximately at a distance of around 545 m from Gunnerus. The compass, heave, pitch, and roll data of Buoy D are publicly available via the Thredds Service at the Norwegian Meteorological Institute [1]. The in-situ wind and current measurements were also available in the buoy database. The buoy is axisymmetric, and its Center of Gravity (CoG) lies at the waterplane/free surface, therefore, coupling of heave motion with pitch and roll modes is inconsequential [5]. Thus, the heave motion is interpreted as the wave elevation time series, measured at a sampling frequency of 2 Hz. Application of 1-Dimensional (1-D) FFT on the wave elevation/heave time series of the buoy gives the 1-D wave frequency spectrum. In this work, Welch's FFT with the Hanning window was applied to the measured wave elevation to compute the wave frequency spectrum. The positions of the vessel and buoy at Breisundet are shown in Fig. 1.

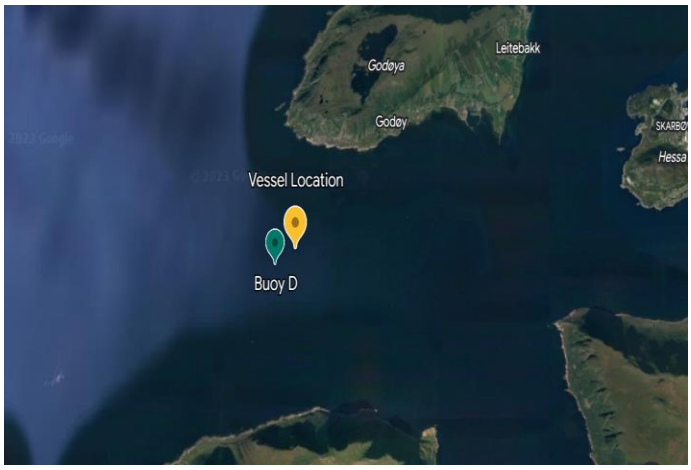

FIGURE 1: THE POSITION OF THE VESSEL AND BUOY D ARE SHOWN USING A GOOGLE EARTH MAP. THE BUOY IS SITUATED AT A DISTANCE OF AROUND 545 M FROM THE VESSEL. THE LOCATION IS THE BREISUNDET STRAIT SITUATED ON THE WEST COAST OF NORWAY.

The radar operates at grazing incidence and covers a range from 250m to 1.65 km of the wave field. Fig. 2 shows the backscattered intensity image. The radius of the blind area (the inside ring) is 250 m. The constant rotation of the radar produces consecutive intensity images of the sea surface for every 2.44 s. The area of each pixel in the image is 4.8 m × 4.8 m. The vessel pole mast obstructed the hind view of the radar which is indicated using black lines in Fig. 2. The sub-image areas within the black lines were not taken into account for the analysis.

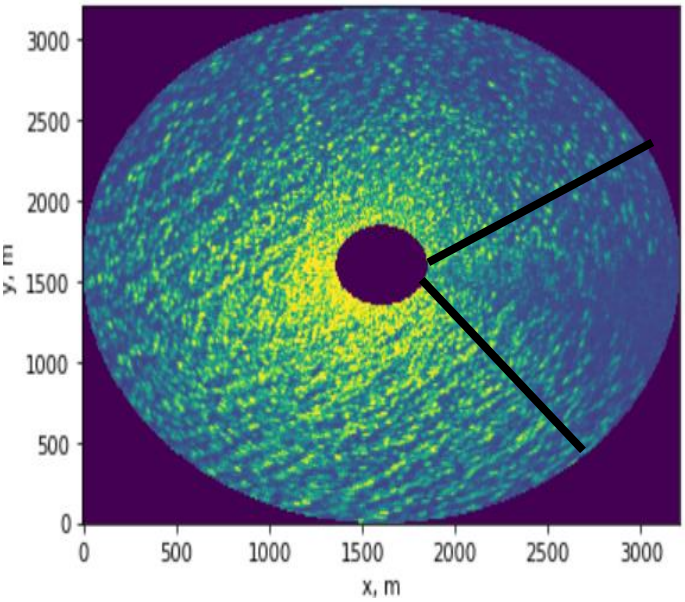

FIGURE 2: BACKSCATTERED INTENSITY IMAGE AT ONE TIME INSTANT. THE YELLOW COLOR REPRESENTS THE HIGH-INTENSITY AREAS. THE GRADUAL CHANGE FROM YELLOW TO BLUE COLOR DENOTES THE LOWERING OF RADAR INTENSITIES. THE INTENSITY IMAGE WITHIN THE BLACKLINES IS BLURRED DUE TO THE VESSEL MAST OBSTRUCTING THE HIND VIEW OF THE RADAR

2.2 Theory of wave spectra

A stochastic free surface elevation $\eta(\boldsymbol{r},t)$ can be written using the following spectral representation [6]

$$\eta(\boldsymbol{r},t) = \sum_{\boldsymbol{k},\omega} e^{i(\boldsymbol{kr}-\omega t)} dZ(\boldsymbol{k},\omega) \tag{1}$$

$\boldsymbol{k} = \{k_x, k_y\}$, is the wave number vector in X and Y directions or the spatial frequencies $k_x = k\,cos\theta, k_y = k\,sin\theta$, and ω denotes the angular frequency. $\boldsymbol{r} = \{x, y\}$ denote the spatial distance in X and Y directions, respectively. dZ is a spectral random variable satisfying the Gaussian probability measure. ω represents the wave frequency. The integral in Eq. (1) is similar to the random-phase/amplitude model of the form.

$$\eta(\boldsymbol{r},t) = \Re[\sum_{\boldsymbol{k},\omega} A(\boldsymbol{k},\omega) e^{i(\boldsymbol{kr}-\omega t+\varphi)}] \tag{2}$$

$A(\boldsymbol{k},\omega)$ is the amplitude spectra. φ represents the random phases distributed uniformly in the interval $\varphi \in [0°, 180°]$, and $\Re$ denotes the real part of the equation. The 3-D wave spectrum $S(k_x, k_y, \omega)$ can be obtained by performing the expectation of dZ with its complex conjugate. $S(k_x, k_y, \omega)$ cannot be directly obtained when applying 3-D FFT to the intensity images. Thus, the procedures given in Sec 2.3 must be followed for obtaining the wave spectra from intensity images.

2.3 Conversion procedures from wave radar images to wave spectra

The step-by-step conversion procedures are listed below:

1) 3D-Fast Fourier Transform (FFT) was applied to the image time series $I(x,y,t)$ to obtain the image power spectra $P(\boldsymbol{k},\omega)$ as per the relation in Eq. (3). F_o is the 3-D Fourier coefficients.

$$F_o(\boldsymbol{k},\omega) = \frac{1}{N_x N_y N_t} \sum_{m=0}^{N_x-1} \sum_{n=0}^{N_y-1} \sum_{l=0}^{N_t-1} I(x,y,t) e^{-i2\pi(x_m k_{x_m} + y_n k_{y_n} + \omega_l t_l)/(N_x N_y N_t)} \tag{3}$$

N_x, N_y, N_t are the number of components along the spatial *x,y,* and time *t* axis. $k_x = \frac{\pi}{\Delta x}, k_y = \frac{\pi}{\Delta y}$, and $\omega = \frac{\pi}{\Delta t}$. Then, the 3-D power spectral density or periodogram is given as

$$P(k_x, k_y, \omega) = \frac{1}{\Delta k_x \Delta k_y \Delta \omega} \left| F_o(k_x, k_y, \omega) \right|^2 \tag{4}$$

where $\Delta k_x = \frac{2\pi}{N_x \Delta x}$, $\Delta k_y = \frac{2\pi}{N_y \Delta y}$, and $\Delta\omega = \frac{2\pi}{N_t \Delta t}$. The low-frequency components (non-homogeneous and non-stationary spectral energy) in $P(k_x, k_y, \omega)$, due to the static dependence of the radar image, were removed using a high-pass filter with a threshold angular cut-off frequency $\omega_{th} = 2\pi \times 0.034$ rad/s and spatial cut-off frequency k_{th}. k_{th} is computed from ω_{th} based on the linear-dispersion relation without the current. The dot product $\boldsymbol{k} \cdot \boldsymbol{U}$ is very small for low wave numbers ($k < k_{th}$) and therefore, the $k_{th} = \frac{\omega_{th}^2}{g}$ can be applied for the lower frequencies [6, 7]. $k = |\boldsymbol{k}|$ is the wave number.

2) The presence of currents causes a Doppler-shift of the linear dispersion shell in the $\boldsymbol{k} - \omega$ plane in an otherwise circular shell of radius $\boldsymbol{k}$. The values of the mean-weighted current vectors [8], $\{U_x, U_y\} \in \boldsymbol{U}$, was derived by minimizing the objective function based on the linear-dispersion relation.

$$f = \sum_{s=1}^{N_s} [\omega_s - \tilde{\omega}(k_{x_s}, k_{y_s}) - \boldsymbol{k} \cdot \boldsymbol{U}]^2 \tag{5}$$

Eq. (5) was solved using the least squares fit [8]. Only

a subset of wavenumber and angular frequency pairs (N_s) corresponding to higher spectral energy, i.e., only the pairs corresponding to a maximum of 25% of the spectral energy, was chosen.

3) The power spectrum $P(\boldsymbol{k},\omega)$ consists of contributions from the currents, sub-harmonics, and super-harmonics. We are mainly interested in the linear dispersion waves, therefore, a band-pass filter, based on the linear dispersion relation, was employed to extract the wave-related components. Further, Borge et al. [4] state that the sub-harmonic and super-harmonic regions in $\boldsymbol{k}-\omega$ plane are contaminated with unknown noise levels in addition to wave energies. Thus, only the wave components associated with the linear dispersion shell were considered.

4) The 3-D spectrum is an even function and symmetric along the ω plane. The filtered wave number-frequency spectrum was integrated over the frequency (ω) axis to obtain the 2-D wavenumber spectrum.

$$P(\boldsymbol{k}) = 2\int_{\omega>0} P(\boldsymbol{k},\omega)\, d\omega \tag{6}$$

5) The backscattered images are affected by different radar modulation mechanisms. One such non-linear modulation mechanism is shadowing. The shorter waves hide behind the longer waves and do not get imaged on the radar. Thus, the small black areas in Fig. 3, also known as non-physical artifacts, are introduced in the backscattered images representing the shadowed waves.

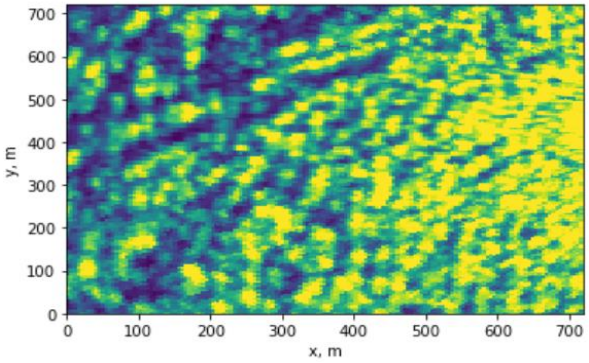

FIGURE 3: BACKSCATTERED INTENSITY IMAGE WITH BLACK AREAS THAT REPRESENT THE SHADOWED AREAS. THE YELLOW COLOR REPRESENTS THE HIGH-INTENSITY AREAS. THE GRADUAL CHANGE FROM YELLOW TO BLUE COLOR DENOTES THE LOWERING OF RADAR INTENSITIES.

For correcting the shadowing modulation, an empirical modulation transfer function was adopted.

$$MTF = |\mathcal{M}(k)|^2 = \frac{S_R(k)}{S_B(k)} \tag{7}$$

$S_R(k)$ and $S_B(k)$ are the 1-D-wave number spectra obtained from the wave radar and buoy, respectively. $S_B(k)$ was calculated using Eq. (8). $S_B\big(\omega(k)\big)$ is the wave frequency spectrum calculated from the buoy measurements.

$$S_B(k) = S_B\big(\omega(k)\big)\frac{d\omega}{dk} \tag{8}$$

The semi-empirical MTF proposed by Borge et al. [4] is given as $|\mathcal{M}(k)|^2 \propto k^{\beta}$. Borge et al. [4] suggested using β=1.2 considering the wave conditions at the Bay of Biscay, which is a swell-dominated area. There are two other modulation mechanisms called tilt and hydrodynamic modulation that affect the intensity spectra at higher wave numbers. On radars operating at grazing incidence, shadowing is the most prominent modulation effect. The tilt and hydrodynamic modulations have minor effects [7].

6) The 3-D amplitude and phase spectra were obtained using the relations in Eqns. (9) and (10). $\Im$ and $\Re$ are used to denote the imaginary and real components, respectively.

$$A\big(k_x,k_y,\omega\big) = \frac{1}{\Delta k_x \Delta k_y \Delta\omega}\big|F_o(k_x,k_y,\omega)\big| \tag{9}$$

$$\varphi\big(k_x,k_y,\omega\big) = tan^{-1}\left(\frac{\Im[F_o(\boldsymbol{k},\omega)]}{\Re[F_o(\boldsymbol{k},\omega)]}\right) \tag{10}$$

Both high-pass and band-pass filtering were applied to the 3-D amplitude spectrum $A(\boldsymbol{k},\omega)$ to remove static patterns and higher-order harmonics, respectively. Subsequently, the filtered amplitude spectrum was factored with the inverse MTF in order to correct for the shadowing modulation effects. Similarly, the phase-spectrum was filtered using high-pass and band-pass filters. However, it was not corrected for modulation effects, as the MTF is a real function. Then, the spectrum $P_{mc}\big(k_x,k_y,\omega\big)$ corrected for the shadowing modulation effects is given as

$$P_{mc}\big(k_x,k_y,\omega\big) = A\big(k_x,k_y,\omega\big)e^{i\varphi(k_x,k_y,\omega)} \tag{11}$$

7) The wave elevation was obtained by applying 3-D Inverse Fast Fourier Transform (IFFT) on Eq. (11). $\widehat{\eta_R}$ represents the complex Fourier coefficients and η_R denotes the wave elevation obtained from the radar images. Inversion using IFFT gives the wave elevation only on the considered spatial and temporal domain.

$$\widehat{\eta_R}(\boldsymbol{r},t) = IFFT\big[P_{mc}\big(k_x,k_y,\omega\big)\big] \tag{12}$$

$$\eta_R(\boldsymbol{r},t) = \Re[\widehat{\eta_R}(\boldsymbol{r},t)] \quad (13)$$

Linear wave equations based on Airy's theory or some higher-order wave theories could be applied for the propagation on spatial and time scales beyond the computational domain. The obtained η_R is not in physical wave scales and needs to be scaled. So η_R was scaled using the relation given in Eq. (14).

$$\eta_{SR}(\boldsymbol{r},t) = \frac{H_{SB}}{4\sigma_R}\eta_R(\boldsymbol{r},t) \quad (14)$$

where η_{SR} is the scaled wave elevation from radar. σ_R represents the standard deviation of the unscaled wave elevation η_R. H_{SB} denotes the significant wave height obtained from a reference station, i.e., from buoy D. In case if no nearby buoy data is available, the reference significant wave height can also be calculated from the Signal-to-Noise ratio of the radar images [9].

8) The physical/scaled wave number-frequency spectrum $S(k_x,k_y,\omega)$ was obtained by applying FFT to $\eta_{SR}(\boldsymbol{r},t)$. The conversion from 3-D wavenumber-frequency spectrum to 2-D directional spectrum is made according to Eq. (15).

$$S(\omega,\theta) = k\frac{dk}{d\omega}\, 2\int_{\omega>0} S(k_x,k_y,\omega)\, d\omega \quad (15)$$

The Jacobian $J = k\frac{dk}{d\omega}$ is the determinant of the matrix $\begin{bmatrix} \frac{\partial k_x}{\partial \omega} & \frac{\partial k_y}{\partial \omega} \\ \frac{\partial k_x}{\partial \theta} & \frac{\partial k_y}{\partial \theta} \end{bmatrix}$, which was applied for converting the spectra from the cartesian coordinate system (k_x,k_y) to the polar coordinate system (ω,θ).The 1-D spectrum $S(\omega)$ was computed by integrating $S(\omega,\theta)$ over the directional axis.

3. RESULTS AND DISCUSSION

3.1 Application of MTF on the wave-number spectra

The buoy and the radar intensity images from 07:00 – 07:40 UTC on 03-04-2022 were considered for the calculations in this section. The extent of the spatial domain considered for each FFT analysis was 480 × 480 m. Many such spatial domains were extracted from the image discs for processing. The maximum temporal extent of the images considered for each FFT analysis is limited to ~ 1 min. Using the least-squares regression algorithm, the following values were estimated for the current velocity components $U_x = 0.095\frac{m}{s}, U_y = 0.108\frac{m}{s}$. The magnitude of the current computed from the radar is 0.140 $\frac{m}{s}$. The magnitude of the current measured using the buoy is around 0.16 $\frac{m}{s}$, which agrees closely with the radar-based estimate. The low values of the current suggest that the Doppler effect induced on the linear dispersion shell may not be significant. These current values were used in designing the band-pass filter based on the dispersion relation, and subsequently, the wave-related components were extracted. The MTF was calculated using Eq. (7) and its inverse was factored with $P(\boldsymbol{k})$. Additionally, the semi-empirical MTF with the coefficient value β=1.2 was also applied to $P(\boldsymbol{k})$. The results of the normalized 1-D wavenumber spectrum are compared in Fig. 4 for different cases.

The shadowing exerts its influence on the wave numbers between 0-0.4 rad/m. The higher wave numbers are governed by the tilt and hydrodynamic modulations. The wave number spectrum based on buoy measurements consists of three major peaks as shown in Fig. 4. To classify the peaks associated with the wind seas and swell, the phase velocity (C_p) of each peak was estimated according to C_p=$\frac{g}{\omega_p}$, ω_p is the peak wave frequency. The phase velocity of the peaks is 14.486 $\frac{m}{s}$, 8.984 $\frac{m}{s}$, and 7.856 $\frac{m}{s}$ corresponding to the wave numbers 0.047, 0.122, and 0.159 rad/m, respectively. The magnitude of the winds measured by the buoy is 10.27 $\frac{m}{s}$. Usually, the swell phase speed is faster than the wind speed, while the phase speed of the wind seas is lower compared to the wind speed. Therefore, we classify that the first peak at 0.047 rad/m corresponds to the swell, and the other two peaks are related to the wind seas.

It is possible to have multiple wind sea systems, e.g., one old wind sea (longer wavelength) and one young wind sea (shorter wavelength). Both wind seas should have been generated locally but the old wind sea has longer fetches (the length of water surface over which wind has blown without obstacles). Breisundet is a narrow strait whose geometry significantly influences the directions of swell and wind seas to be aligned along the strait's axis.

The radar-based spectrum shows considerable deviation from the buoy-based spectrum especially at the peaks before applying MTF. The application of MTF improves the overall calculations of the wave radar spectrum between 0.05-0.25 rad/m, though there are slight discrepancies at the lowest wave numbers and the peaks related to wind seas. No improvements in the spectral estimations in the higher wave numbers could be seen after the application of MTF. This is due to the domination by tilt and hydrodynamic modulation effects in these regions. The deviations were still considerable within 0-0.4 rad/m when applying the semi-empirical MTF. Further, it takes away more energy from the radar-based spectrum at the higher wave numbers. Since the shadowing is a highly non-linear mechanism depending on different factors and sea states, usage of the semi-empirical MTF did not give accurate results for our case. The filtered + MTF corrected spectra shown in Fig. 4 are not scaled yet. The effects of applying MTF on the scaled wave frequency spectrum are illustrated in Sec. 3.2.

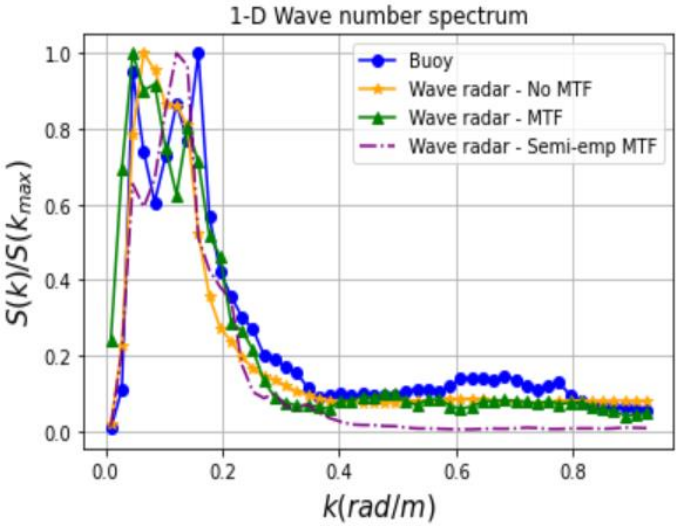

FIGURE 4: THE RADAR-BASED FILTERED WAVENUMBER SPECTRA ARE CORRECTED FOR SHADOWING MODULATION USING MTF AND COMPARED WITH THE BUOY-BASED SPECTRUM. THE MEASUREMENTS CORRESPONDING TO 07:00-07:40 UTC WERE UTILIZED.

3.2 Comparison between the wave frequency spectrum from the radar and buoy

Using the computed MTF, the procedures 6) – 8) in Sec. 2.3 were applied to estimate the 1-D wave frequency spectrum from the wave radar. The processed spectra were compared with the spectra estimated from the buoy in Fig. 5 and Fig. 6. The two figures correspond to periods between 07:00-07:40 and 08:00-08:40 UTC, respectively. The 1-D wave spectrum from the buoy was regarded as the truth.

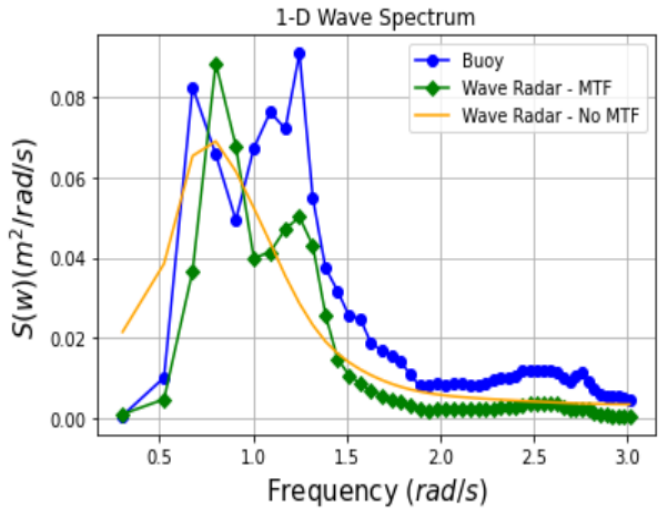

FIGURE 5: SCALED RADAR-BASED WAVE SPECTRUM IS COMPARED WITH THE SPECTRUM FROM THE BUOY. THE MEASUREMENTS CORRESPONDING TO 07:00-07:40 UTC WERE UTILIZED.

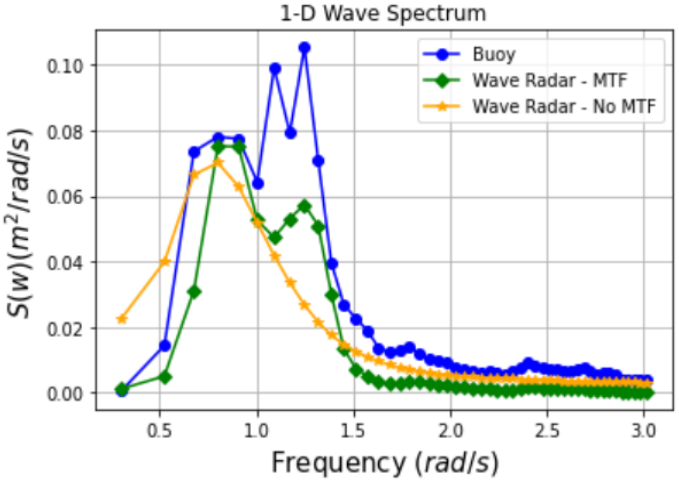

FIGURE 6: RADAR-BASED WAVE SPECTRUM IS COMPARED WITH THE SPECTRUM FROM THE BUOY. THE MEASUREMENTS CORRESPONDING TO 08:00-08:40 UTC WERE UTILIZED.

The radar-based spectrum without applying MTF deviates from the measured spectrum considerably in both cases. The application of MTF greatly improves spectral estimation. The estimate of the swell peak matches the buoy measurements closely. However, a noticeable underestimation of energy at the wind-wave peaks could be observed. Especially, the radar-based spectrum could not resolve the peak at 1.1 rad/s. Additionally, the spectrum measured from the buoy possesses a modest amount of additional energy in the high-frequency region which the radar-based spectrum with MTF could not capture.

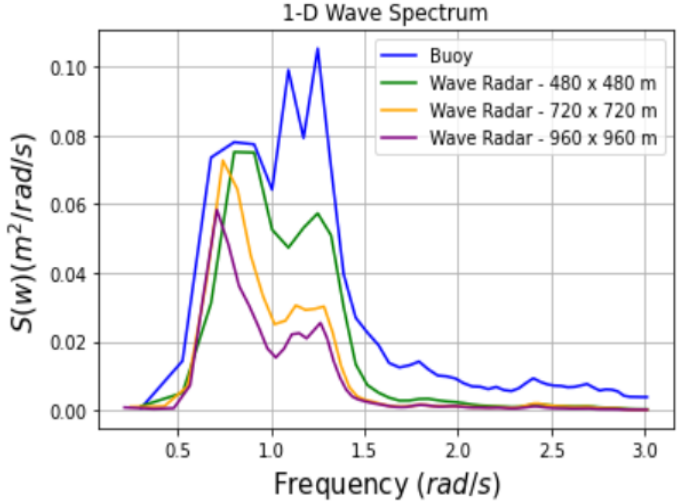

FIGURE 7: SPATIAL DOMAINS OF THREE DIFFERENT SIZES WERE EXTRACTED FROM THE RADAR IMAGES AND APPLIED FOR POST-PROCESSING. THE RESULTING WAVE SPECTRA CORRESPONDING TO EACH SIZE ARE COMPARED. THE MEASUREMENTS CORRESPONDING TO 08:00-08:40 UTC WERE UTILIZED.

It was presumed that the discrepancy at the peaks related to wind waves could be connected with the spatial domain considered during the FFT analysis. Fig. 7 illustrates this effect.

The areas in the intensity image discs were extracted using boxes of three different spatial sizes 480 × 480 m, 720 × 720 m, and 960 × 960 m. The same temporal extent of 1 min was considered.

The domain with a spatial extent of 480 × 480 m gives the best results in terms of quantifying the swell peak and partially the wind-sea-induced peak, as given in Fig. 7. The usage of larger spatial domains deteriorates the radar-based spectral estimate at all the peaks.

3.3 Effects due to range dependency on the spectral estimation

The intensity of the electromagnetic waves decreases with the increase in range, and consequently, the estimated wave spectra vary with different ranges. From the image discs, boxes of size 480 × 480 m were extracted from the near range (260-740m), mid-range (590-1070m), and far range (850-1330m). Then the wave spectra were estimated for each of these ranges to study the effect of range dependence. The results are presented in Fig. 8. The spectrum corresponding to the mid-range seems to produce at least two peaks and matches the buoy-based spectrum to some extent. Still, the peak at 0.122 rad/m could not be resolved. The spectra from the other two ranges show noticeable deviation at the peak. The near-range spectrum has some more energy at the higher wave numbers (≥ 0.8 rad/m) than that of the buoy. This could be associated with the tilting mechanism related to low incidence angles. The far-range spectrum possesses nil energy at the higher wave numbers. Fig. 9 displays the MTF curves estimated using Eq. (7) for the three considered ranges. The curves differ with respect to the three ranges. This is indicative of the fact that a single semi-empirical MTF might not be valid for the entire range for correcting the shadowing modulation. The shadowing effect can be minimal at the near-range, while the far-range can be more prone to shadowing.

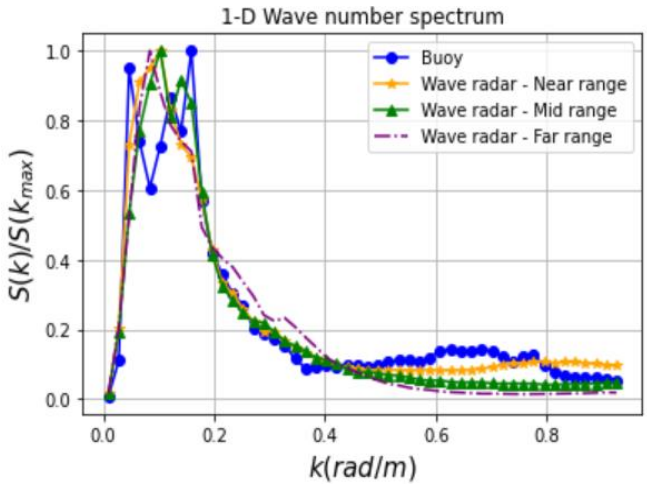

FIGURE 8: COMPARISON BETWEEN THE RADAR-BASED SPECTRA OBTAINED AT NEAR- RANGE, MID-RANGE, AND FAR-RANGE. THE PRESENTED RESULTS ARE BEFORE APPLYING MTF. THE SPECTRUM FROM THE BUOY IS CONSIDERED AS THE REFERENCE.

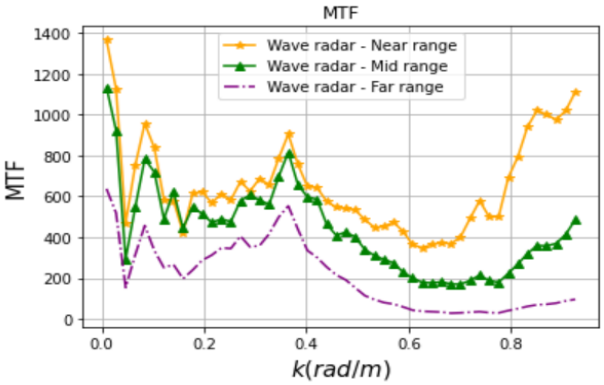

FIGURE 9: SHOWS THE MTF ESTIMATED USING EQ. (7) FOR CORRECTING SHADOWING EFFECTS FOR THREE DIFFERENT CASES.

4. CONCLUSION

The back-scattered intensity images collected during the full-scale trials at Breisundet were used to process the wave spectra based on the inversion scheme proposed by Borge et al. [4]. The tests were conducted close to a wave buoy whose measurements were utilized to estimate MTF in order to correct the shadowing effects, scale the wave elevation, and validate the radar-based wave spectrum.

It was comparatively shown that the application of MTF, estimated using Eq. (7), improves the resulting spectral estimation compared to the case without MTF, and also compared to the correction based on semi-empirical MTF. Borge et al. [4] derived the semi-empirical formulation for MTF for sea states prevalent along the Northern Coast of Spain, which still needs to be modified to account for different sea conditions and other factors. For instance, the MTF curves varied with different ranges. So, having a unified exponent in the semi-empirical MTF for all ranges might be problematic. The exponent must be modified in accordance with the range. The comparison of the spectrum corresponding to different ranges showed that the mid-range spectrum gave better results.

The scaled wave spectrum from the radars gave better agreement with the buoy-based spectrum at the swell peak. However, some errors could be noticed at the peaks corresponding to wind seas. The estimation can still be improved through the proper choice of spatial domains. The underestimation of wind sea peaks can also be partly associated with the scaling formulation based on the total significant wave height. The possibility of applying different scaling factors corresponding to wind and swell seas must be investigated.

In this work, the accuracy of the inversion of wave spectra from radar images was studied through comparison with the buoy data. Further work will be done to compare the wave elevation time series estimated from the radar with the buoy measurements. Fig. 10 and Fig. 11 show the scaled phase-resolved wave elevation and the equivalent raw backscattered intensity images, respectively. The spatial domain of 720 × 720 m was applied as a basis for the FFT processing of the wave elevation.

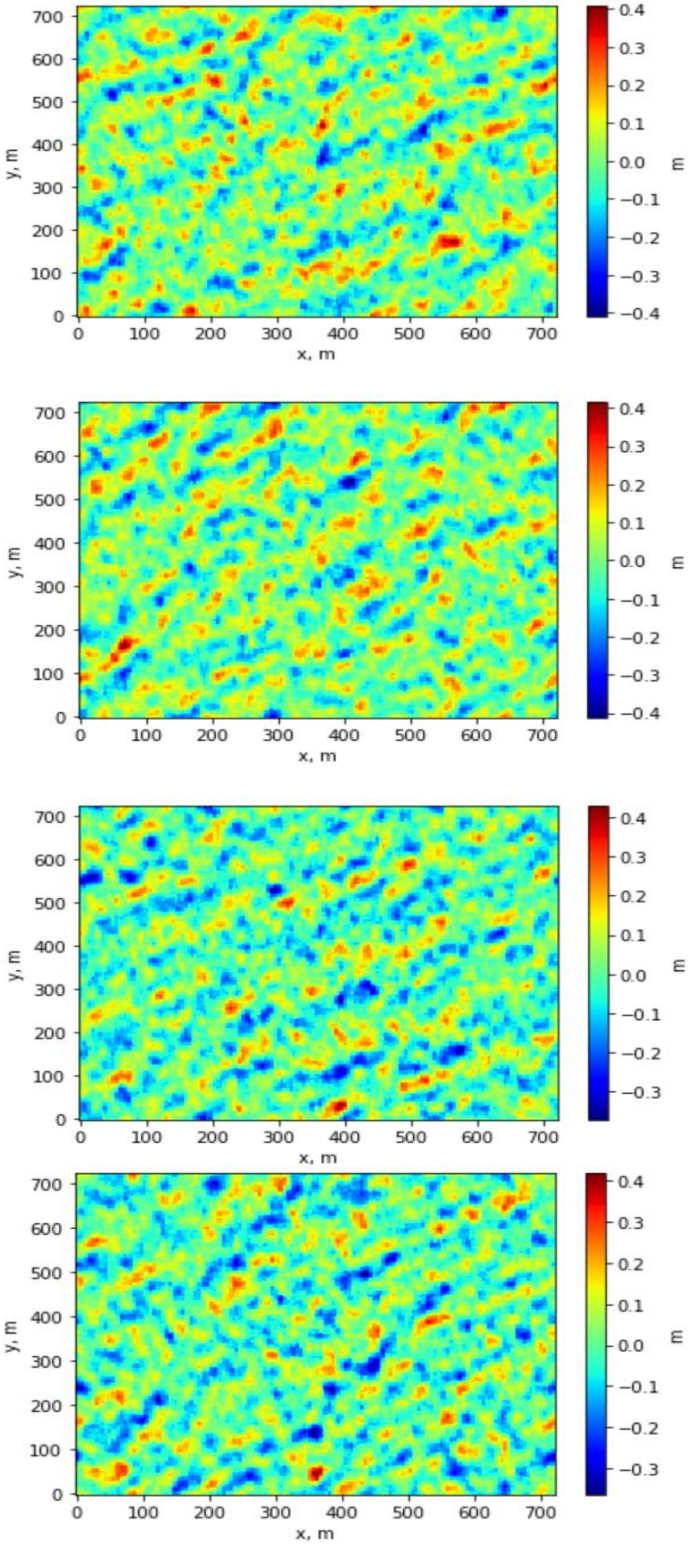

FIGURE 10: PHASE-RESOLVED WAVE ELEVATION AT FOUR CONSECUTIVE TIME STEPS.

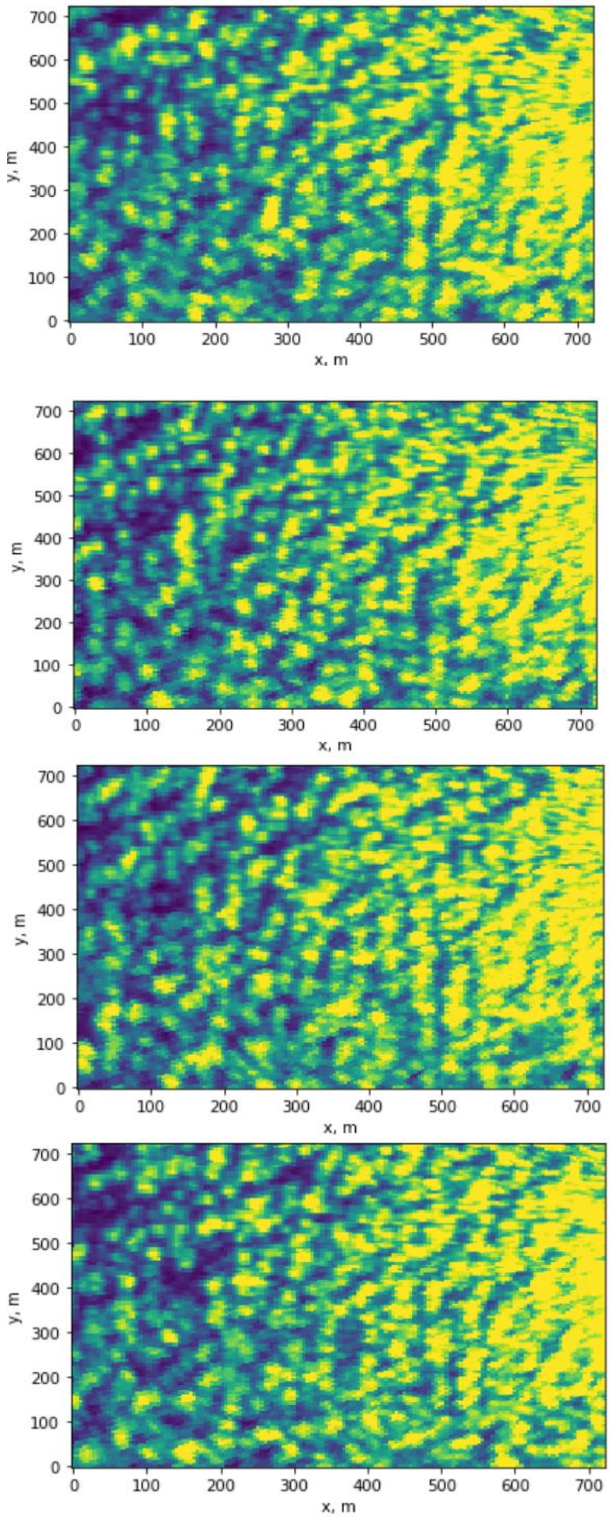

FIGURE 11: CONSECUTIVE BACKSCATTERED INTENSITY IMAGES WITH EQUIVALENT SPATIAL AND TIME SCALES TO THOSE IN FIGURE 10.

ACKNOWLEDGEMENTS

This work was made possible through the Centre for Research-based Innovation MOVE, financially supported by the Research Council of Norway, NFR project no. 237929 and the consortium partners, http://www.ntnu.edu/move. Wim Lavrijsen, AIDE-QC, Lawrence Berkely National Laboratory, is sincerely thanked for providing the Python wheels for Nomad 4 c++ library.

REFERENCES

[1] B. R. Furevik, L. Lønseth, A. L. Borg, V. Neshaug and M. Gausen, "Oceanographic observations for the Coastal Highway E39 project in Mid-Norway," The Norwegian Meteorological Institute, 2016.

[2] H. E. Krogstad and S. S. Barstow, "Satellite wave measurements for coastal engineering applications," *Coastal Engineering,* no. 37, pp. 283-307, 1999.

[3] k. Christakos, Z. Gao, B. R. Furevik, J.-V. Bjorkqvist and O. J. Aarnes, "In situ coastal observations of wave homogeneity and coherence.," *Applied Ocean Research,* no. 129, pp. 1-14, 2022.

[4] J. C. N. Borge, G. Rodriguez, K. Hessner and P. I. Gonzalez, "Inversion of Marine Radar Images for Surface Analysis," *Journal of Atmospheric and Ocean Technology,* 2004.

[5] S. F. Barstow and H. E. Krogstad, "General analysis of directional ocean wave data from heave/pitch/roll buoys," *Modeling, Identification and Control,* vol. 5, no. 1, pp. 47-70, 1984.

[6] J. N. Borge and C. G. Soares, "Analysis of directional wave fields using X-band navigation radar," *Coastal Engineering,* no. 40, pp. 375 - 391, 2000.

[7] S. Støle-Hentschel, J. Seeman, J. C. N. Borge and K. Trulsen, "Consistency between Sea Surface Reconstructions from Nautical X-band Radar Doppler and Amplitude Measurements," *Journal of Atmospheric and Oceanic Technology,* 2018.

[8] I. Young and W. Rosenthal, "A Three-Dimensional Analysis of Marine Radar Images for the Determination of Ocean Wave Directionality and Surface Currents," *Journal of Geophysical Research,* vol. 90, pp. 1049-1059, 1985.

[9] J. Nieto-Borge, K. Hessner, P. Jarabo-Amores and D. d. l. Mata-Moya, "Signal-to-noise ratio analysis to estimate ocean wave heights from X-band marine radar image time series," *IET Radar Sonar Navigation,* vol. 2, no. 1, pp. 35-41, 2008.